2015 IEEE/RSJ International Conference on Intelligent Robots and Systems (IROS)
Congress Center Hamburg
Sept 28 - Oct 2, 2015. Hamburg, Germany

Dynamic Obstacle Avoidance for Bacteria-Powered Microrobots*

Hoyeon Kim, U Kei Cheang, A. Agung Julius, and Min Jun Kim, *Member, IEEE*

Abstract— **As microscale robots are becoming increasingly popular due to their potential for medical and industrial applications, various designs of microscale robotic system have been developed. However, there has not been much work on autonomous control algorithms for microscale robots in microfluidic environments. In this paper, we introduce an autonomous navigation algorithm for the bacteria-powered microrobots (BPMs) in a workspace with moving obstacles. A BPM consists of a rigid inorganic body with bacteria attached on the surface. The attached bacteria provide propulsive force and are controllable using electric fields, which had been demonstrated in previous work. We take the controllability of BPMs and the unpredictable motion of dynamic obstacles into account to develop a dynamic obstacle avoidance approach. Moreover, we use finite element simulation to observe an electric field around a moving obstacle to model the field's deformation. Demonstration of dynamic obstacle avoidance approach through simulation results and experimental data are presented in the paper.**

I. INTRODUCTION

Microrobots have been shown to be capable of conducting microscale tasks such as drug delivery, cell manipulation, microassembly, and biosensing [1-4]. As an example, *in vitro* targeted delivery was demonstrated using magnetotactic bacteria under a gradient DC magnetic field in a clinical magnetic resonance imaging system [5]. Others have also explored microrobots for transporting cargos such as chemicals and live cells using magnetic fields [6, 7]. Furthermore, microgrippers have been used to improve the functionality of microrobots [8-11]. All of these technologies have the potential to be utilized for enhancing the effectiveness of medical treatments and manufacturing tools by localizing the operations at the selected target area.

There are several studies inspired by microorganisms such as flagellated bacteria for using their capability to swim at low Reynolds number [12-18]. In this environment, viscous forces dominate and a swimmer must use nonreciprocal motion for locomotion; one such example is the rotating motion of the bacterial flagella [19]. Bacterial flagella rotate clockwise (CW) and counterclockwise (CCW) to move forward and change swimming direction, respectively [20]. Bacteria attached to the surface of microfabricated parts, referred to as bacteria-powered microrobots (BPMs), are shown to naturally impart a predominantly rotational motion, largely due to the result of the massive arrays of flagella working cooperatively on a monolayer of swarming bacteria [21]. The BPMs used in this paper utilize a hybrid actuation system, in which we exploit both the natural motility of the bacteria and electrophoretically induced mobility by a DC electric field.

The intrinsic motion of BPMs and the motion control of BPMs are described in our previous work [16, 18, 22]. The application of BPMs such as phenotypic biosensing and visual-based feedback control of micromanipulation had been exploited as well [16, 22]. For the BPMs to perform more complicated tasks, such as micro-assembly and manipulation, the use of an autonomous navigation system will be essential in environments with various obstacles in order to allow the BPMs to complete their missions without collision. In particular, the dynamic obstacles will increase collision risk and stop the BPMs from finishing tasks. In addition, the autonomous navigation will help BPMs to save energy and time to approach the goal position. To address scenarios where obstacles are moving, we developed a dynamic obstacle avoidance algorithm. The algorithm is based on our previous work with static obstacles [23]. In addition, numerical simulations and experiments were carried out to show the feasibility of our algorithms.

The first section of this paper reviews the kinematic model of the BPMs. The next section describes the dynamic obstacle avoidance approach. The last section demonstrates the approach in simulations using random parameters and in a real experiment.

II. BACTERIA-POWERED MICROROBOTS (BPMS)

A. Cell Culture and Preparation of BPMs for Experiment

BPMs were manufactured by blotting *Serratia marcescens* onto the surfaces of SU-8 structures. *S. marcescens* were cultured on an agar plate which was prepared by pouring 30 ml of the agar solution (1.5 g Difco Bacto agar, 1.25 g yeast extract, 1.25 NaCl, 2.5 g trypton, and 600 ml of 25% glucose solution into 250 ml of deionized water) into a 15 cm Petri dish. Once the agar solution solidifies into gel, 5 µl of *S. marcescens* was inoculated on the edge of the agar plate. The inoculated agar plate was placed inside the incubator at 34°C for 12 hours to create a swarming colony. SU-8 structures were blotted on the edge of the colony.

B. Fabrication of BPMs

The BPMs are fabricated by attaching bacteria onto untethered microstructures. First, a water-soluble dextran sacrificial layer is spin-coated on a substrate by procedure. Then a 3µm layer of SU-8 is spin-coated on top of the dextran layer and made into rectangular microstructures (30 µm × 32 µm) using photolithography. Bacteria are attached using a blotting method in which the microstructures are inverted onto a swarm plate of *S. marcescens*. Bacteria attach favorably to

*Research supported by National Science Foundation and U.S. Army Research Office.

Hoyeon Kim, Department of Mechanical Engineering and Mechanics, Drexel University, Philadelphia, PA 19104, U.S.A. hk453 @coe.drexel.edu

U Kei Cheang Department of Mechanical Engineering and Mechanics, Drexel University, Philadelphia, PA 19104, U.S.A. ukc23 @coe.drexel.edu.

A. Agung Julius, Department of Electrical, Computer and Systems Engineering, Rensselaer Polytechnic Institute, Troy, NY 12180, U.S.A. agung@ecse.rpi.edu

Min Jun Kim, Department of Mechanical Engineering and Mechanics, Drexel University, Philadelphia, PA 19104, U.S.A. mkim@coe.drexel.edu

the microstructure upon physical contact due to the polysaccharide-rich pink slime produced by swarmer cells of *S. marcescens*. Once blotted, the microstructures are placed inside of a water-filled test chamber where the dextran layer is dissolved, thus, releasing the blotted microstructure. The released blotted structures are BPMs. Fig. 1(a) shows a BPM after blotting and releasing. The randomly distributed long rods are the bacteria, as shown in Fig. 1(a). On the surface of the BPM is a monolayer of highly packed swarmer bacterial cells, which is called as bacterial carpet. The use of bacteria as the motion actuators reduces the cost and complexity of the fabrication procedure. Furthermore, the negative charged bodies of *S. marcescens* are ideal for controlling BPMs using electrical stimulation.

C. Kinematic Model for BPMs

When released in fluid, a BPM exhibits self-actuated rotational motion presumably due to large-scale global coordination of bacterial carpet flagella [24]. The motion of the self-actuated structure has two distinct velocity components, translational and rotational, which depends on x-axis and y-axis position in the local coordinate frame with respect to its center of mass [18]. The equations of translation are given as follows:

$$\mathrm{V_x} = \bar{p}\beta_1, \ where \ \ \beta_1 := \frac{1}{k_T}\sum_{i=1}^{N_b}\cos\theta_i \tag{1}$$

$$\mathrm{V_y} = \bar{p}\beta_2, \ where \ \ \beta_2 := \frac{1}{k_R}\sum_{i=1}^{N_b}\sin\theta_i \tag{2}$$

where N_b is the number of bacteria that are attached, and k_T and k_R are the translational viscous drag coefficient and the rotational viscous coefficient respectively.

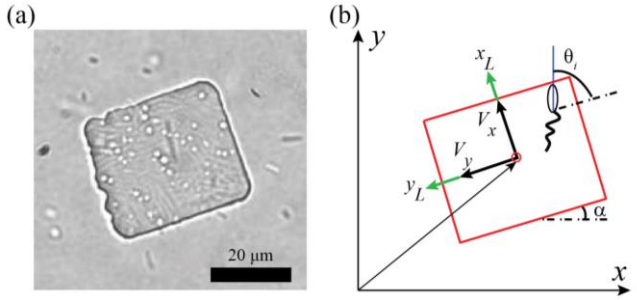

Figure 1. BPM kinematic system coordinates (a) Bacterial carpet on the structure, (b) A schematic of the BPM.

Fig. 1(b) indicates the coordinate system for (1) – (3). The velocities are proportional to the mean of propulsion forces $\bar{p}$ and $\beta_{1,2}$. The parameters $\beta_{1,2}$ are related to the amount of attached bacteria and their respective orientation θ_i. Furthermore, the rotation is defined as follow:

$$\Delta\alpha = \bar{p}\beta_3, where \ \ \beta_3 := \frac{1}{k_R}\sum_{i=1}^{N_b}\left(b_{i,x}\sin\theta_i - b_{i,y}\cos\theta_i\right) \tag{3}$$

where b_i is the vector of i-th bacterium in the local body-fixed coordinate. Combining with a stochastic model for electrokinetic actuation in previous work [25], we can describe the BPM's position, using a global coordinate system, as follows:

$$\begin{pmatrix} x_i \\ y_i \\ \alpha_i \end{pmatrix} = \begin{pmatrix} x_{i-1} \\ y_{i-1} \\ \alpha_{i-1} \end{pmatrix} + \begin{bmatrix} \cos\alpha & -\sin\alpha & 0 \\ \sin\alpha & \cos\alpha & 0 \\ 0 & 0 & 1 \end{bmatrix} \begin{bmatrix} V_x \\ V_y \\ \Delta\alpha \end{bmatrix} t + \begin{pmatrix} U_x \\ U_y \\ 0 \end{pmatrix} \beta_4 \tag{4}$$

where U_x and U_y are the input voltages for x direction and y direction respectively, β_4 is related to the charge of cell bodies that causes the electrophoretic force. The velocity of the BPM is proportional to the magnitude of the applied voltages. The displacement at instantaneous input voltages is estimated by β_4. We can evaluate V_x, V_y, and $\Delta\alpha$ as follow:

$$\begin{bmatrix} V_x \\ V_y \\ \Delta\alpha \end{bmatrix} = \bar{p} \begin{bmatrix} \beta_1 \\ \beta_2 \\ \beta_3 \end{bmatrix} \tag{5}$$

Through the kinematic model of the BPM, the trajectory was calculated by U_x and U_y continuously and our proposed obstacle avoidance method calculates the input voltage U_x and U_y at present situation. The kinematic modeling of BPMs can be useful to develop robotic algorithms with high reliability.

D. Validation and Simulation Configuration

The kinematic model, as shown in (4), was verified by comparison between the estimated position of the BPM from the motion model and experimental data from tracking [26]. The errors for the x and y positions are 0.02 ± 0.92 μm and 0.22 ± 1.13 μm, respectively, indicating the simulation closely matched the experimental values (Fig. 2).

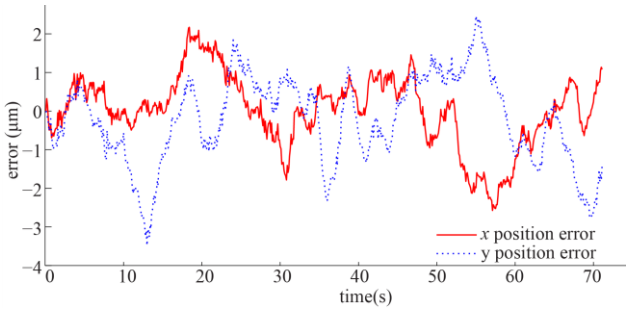

Figure 2. Comparison in errors between the real motion of the BPM and the model.

To simulate the proposed approach in Section IV, the model of the BPMs was used to calculate the corresponding position under the control inputs determined by our algorithms. The required parameters including β_1, β_2, β_3, and β_4 were randomly chosen and the size of BPM is the same as the BPMs from the experiments. The dynamic obstacles are controlled manually during the simulation.

III. DYNAMIC OBSTABLE AVOIDANCE APPROACH

The motion planning in dynamic environment is based on the Dynamic Window Approach (DWA) [27] and the Vector Field Histogram (VFH) [28] approach. An additional objective function was added in the resultant objective function to achieve accurate motion control. VFH is also utilized to restrict the range of control input from DWA which heads to dynamic obstacles.

A. Considering Constraint Elements for Control of BPMs

The motion planning algorithm reflects several constraint elements with regard to the characteristics of BPMs and their electrophoretic mobility under an electric field in order to perform optimal motion control. First, the motion of BPMs is omnidirectional which means that they can move in any direction in accordance with the applied electric field. Second, the natural motion of the BPMs, described as self-actuation, is

not controllable and varies among BPMs [16, 18, 22]. This inherent uncontrollable motion increases the probability of collision with the dynamic obstacles. To address this concern, a robust kinematic model for a BPM which accounts for this self-actuation behavior is reflected on the control input to reduce the probability of collision by predicting the next displacement of a BPM after $\beta_1, \beta_2, \beta_3$ are determined by observing the motion of a BPM. Third, the applied electric field will be distorted around the dynamic obstacles. This deformation could result in undesired motion when a BPM is located on the deformed electric field. To verify this issue, we simulated an electric field with moving obstacle using COMSOL Multiphysics (Fig. 3) and characterize the deformation.

The simulation results of COMSOL enable us to model an electric field around the boundaries of a circular dynamic obstacle, as shown in Fig. 3. The electric field (10 V/cm) was applied in the *x*-direction. A moving mesh was used to simulate the movement of the dynamic obstacle in the *–x* direction with a speed of 10 μm/s. In the simulation, we regarded the obstacle as an insulator. The direction of the electric field is represented by arrows at 0s, 10s, and 20s respectively in Fig. 3. The electric field was deformed around the obstacle and the most of distortion happened in front of the obstacle and behind of the obstacle.

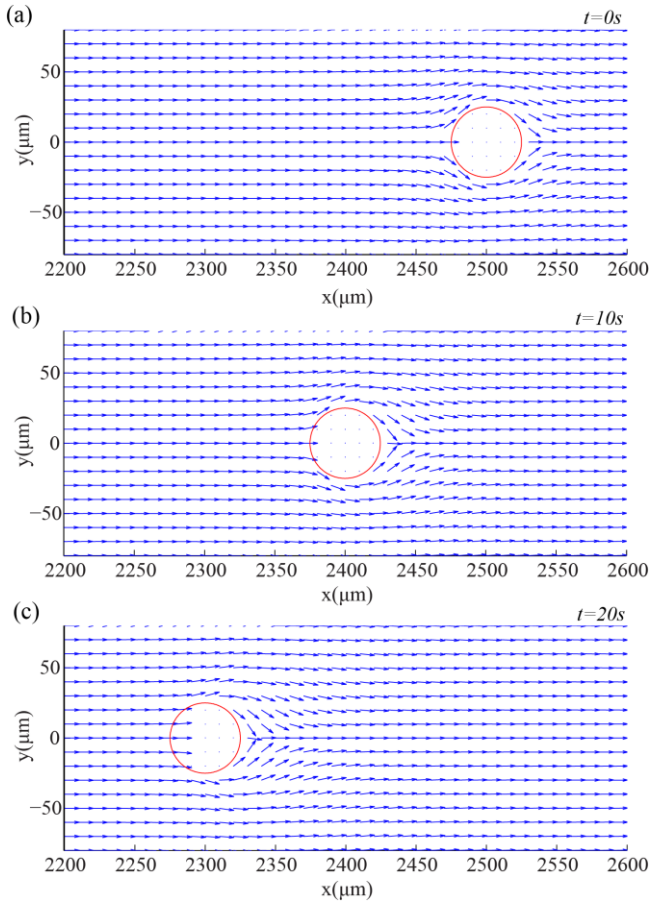

Figure 3. COMSOL Multiphysics simulation results. (a) Electric potential flow at 0s, (b) 10s, and (c) 20s.

To ensure the BPMs follow the desired control input, the deformed area should be avoided so that the BPMs can be steered to the desired direction instantly. As the dynamic obstacle continues to be moving, the deformed electric potential area becomes conical shaped in front of the obstacle, as shown in Fig. 4(c). The affected area gets wider behind the obstacle (Fig. 4).

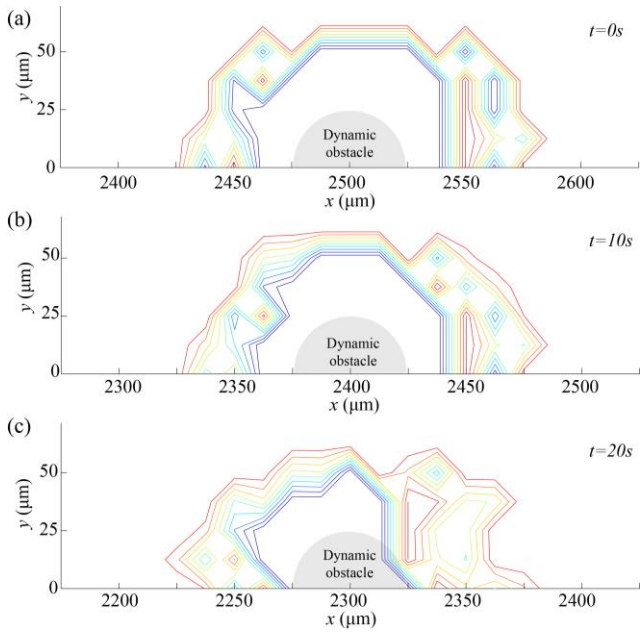

Figure 4. COMSOL Multiphysics simulation results. (a) Non-uniformity of electric potential field at 0s, (b) Non-uniformity of electric potential field at 10s, (c) Non-uniformity of electric potential field at 20s.

B. Proposed Approach to Avoid Dynamic Obstacles

We combine the Dynamic Window Approach (DWA) and Vector Field Histogram (VFH) methods together for dynamic obstacle avoidance using a single BPM. Using the two approaches, the navigation algorithm prioritizes eliminating collisions with obstacles and searching for an optimal input. The constraint elements, mentioned above, are included in the objective functions which are *head*, *clearance*, *velocity,* and *control* functions. Each objective function calculates the most valuable control input for each purpose and the resultant control input is decided from an integral function which consists of these four functions. The *control* function is designed to take into account the controllability we defined as the ability to follow the electric field. However, even though the proposed objective function computes the safe motion control input using *clearance* function, the dynamic obstacles can promote collisions due to their unpredicted motion. Thus, we utilized VFH approach as a complementary method to prevent collision from moving obstacles. The redefined VFH in our algorithm is to drive a BPM toward less cluttered spaces by restricting the control inputs that cause the BPM to head toward obstacles.

Comparing with previous work [23], this VFH approach excludes all inputs that return a heading direction toward obstacles. Then, the implemental control input has been chosen from our objective function. This method is repeated until the BPM reaches a goal position.

C. Explanation of Main Function

In case of the objective function for the DWA, the main objective function is composed of four sub-functions that

represent each expected outcome: orientation towards the target position (*head*), movement by input (*movement*), collision clearance (*clearance*), and the controllability of the BPM (*control*). It is given as follows:

$$f(U_x, U_y) = \alpha \cdot head(U_x, U_y) + \gamma \cdot movement(U_x, U_y) + \omega \cdot clearance(U_x, U_y) + \delta \cdot control(U_x, U_y) \quad (6)$$

where, the U_x and U_y are input voltages on *x*-axis, and *y*-axis respectively.

The *head* function is used to represent the alignment of a BPM with the goal direction. The function is calculated from the angle Φ between two vectors, υ and ρ (Fig. 5(a)), which are the direction vector from current position to next position by input U_x, U_y, and the direction vector from next position to goal pose, respectively. The closer Φ is from 180°, the larger the cost of head function become. The return values of the *head* function are represented by H_{cost} in Fig. 5(c). Consequently, the *head* function works for a BPM to move toward the goal position.

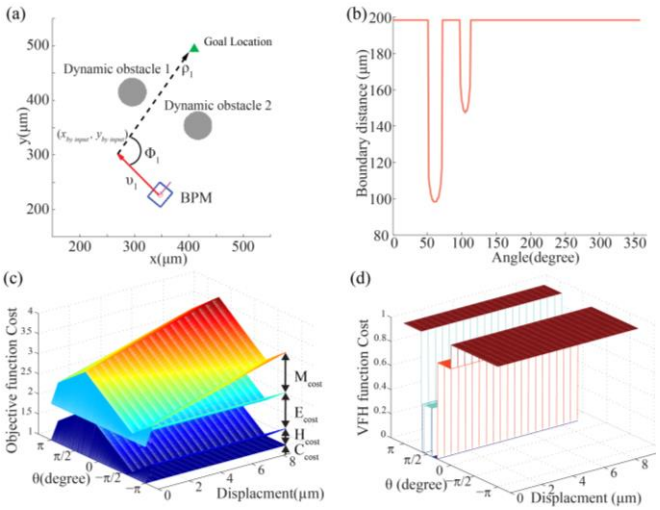

Figure 5. Scheme of our approach. (a) Obstacle occupied situation and *head* cost, (b) Boundary information around BPM at (a), (c) Integral objective function cost, (d) VFH approach. (C_{cost} : *clearance*(U_x,U_y), H_{cost} : *head*(U_x,U_y), M_{cost} : m*ovement*(U_x,U_y), E_{cost} : *control*(U_x,U_y))

The *movement* function measures the displacement of the BPM using the control input value at a chosen sampling time. High voltage input generates a long displacement. The cost of *movement* is given as follows:

$$movement(U_x, U_y) = \beta_4 \sqrt{U_x^2 + U_y^2} / dist_{max} \quad (7)$$

where $dist_{max} = \beta_4 \sqrt{U_{max_x}^2 + U_{max_y}^2}$ is the maximum movement by the maximum input voltage U_x and U_y.

The *control* function evaluates the predicted controllability through the electric field at the predicted position by U_x, U_y. It is difficult to recalculate intrinsic electric potential every sequence because the intrinsic electric potential is changed when dynamic obstacle moves. Thus, we used the characteristics of potential field around obstacles. The gradient potential caused by deformation of the electric field is characterized through the COMSOL Multiphysics simulation. Using the gradient profile around obstacles, the *control* function calculates the distortion of electric force based on the gradient potential at the predicted position. Therefore, the cost will be higher at the area where high gradient potential exists. The resultant cost from the *control* function is indicated as E_{cost} in Fig. 5(c).

The *clearance* function is to determine the collision probability for a trajectory. In our algorithm, the boundary distance (BD) from the center of a BPM is used to check whether the BPM collides with dynamic obstacles at the resultant motion. Using the BD, we can identify the occurrence of a collision with an obstacle at the predicted position. Fig. 5(b) shows the boundary information of the scenario in Fig. 5(a) within a 200 μm range with respect to 0~360º. The *clearance* cost measures the shortest distance from the BPM to obstacles while considering movement from self-actuation. The *clearance* cost is 1 in the case of no collision (Fig. 5(a)) and 0 for a collision.

At last, those components will be normalized to [0,1]. The result of four objective functions is described in Fig. 5(c) and the control input is selected by choosing the highest cost value from the sum of each objective cost. The peak of the objective function can be changed depending on the weighting parameters α, β, γ, and ω. In Fig. 5(c), the weight values are equal and the direction of final control input is 87º. However, even if the determined motion control made no collision at next position, BPM would be close to the area occupied by two dynamic obstacles and collision might be expected. To make sure that a BPM stays out of the occupied area in the future. As a result of the VFH method, we can exclude the control inputs between 50 ~ 110º in Fig. 5(d) and prevent the BPM from heading towards the dynamic obstacles in advance. Thus, the optimal input voltage of rest control space, which is not excluded by VFH method, will be obtained from the main objective function.

IV. SIMULATION AND EXPERIMENTAL RESULTS

We demonstrate the feasibility of our obstacle avoidance algorithm using simulations and experiments. In the simulations, we used several parameters to simulate our algorithm and the chosen parameters matched that of the experiments. Moreover, standard deviations of 1.5, 1.3, 0.09, and 0.06 for parameters β_1, β_2, β_3, and β_4, were used in the normal probability distribution model respectively to compute BPM locomotion with a mean propulsion, $\bar{p}$ of 0.41 *pN* in our simulation. The input velocity space is related to voltage ranges which have an upper limit of 20 V. The experiment is done using a vision-based system. The dynamic obstacles are not affected by the electric field. The sampling time was 0.16s for both simulations and experiments.

A. Simulation Result

We simulated the dynamic obstacle avoidance method using circle shape obstacles in 2D with various parameters to investigate the reactivity of the objective function. The parameters are 0.5 for β_1, 0.7 for β_2, 0.51 for β_3, and 0.44 for β_4. The performance of the obstacle avoidance depends on the weighting parameters. We focused on the functionality of the *control*, *head*, and *clearance* functions. Fig. 6 illustrates the resultant path based on the varied weights. In these sets of

simulations, α, ω, and δ were varied. The parameter γ was held near constant since it affects mainly velocity and has little impact on the final trajectory. In order to properly compare performance based on different weight values, all of the simulations used performed using the same trajectory of the dynamic obstacle.

In the first simulation, which also serves as the control, the dynamic obstacle moved at a speed of 5 µm/s using manual control from the time between t_0 and t_3 (red circle). The weighting of *head* function is 0.5. In the next simulation, the weights of the *head* and *control* functions were decreased to 0.3 and increased to 0.7, respectively. As a result, the motion planning of the BPM had a wider trajectory (blue triangle in Fig. 6(a)). The trajectory (blue triangle) in Fig. 6(a) did not move into the deformed area. The BPM kept moving forward left (asterisk in Fig. 6(a)) because of the low cost of *head* function with high *clearance* cost. When dynamic obstacle turns right at t_2, the BPM begins to head to the goal position from t_2^* to t_4^* (Fig. 6(a)).

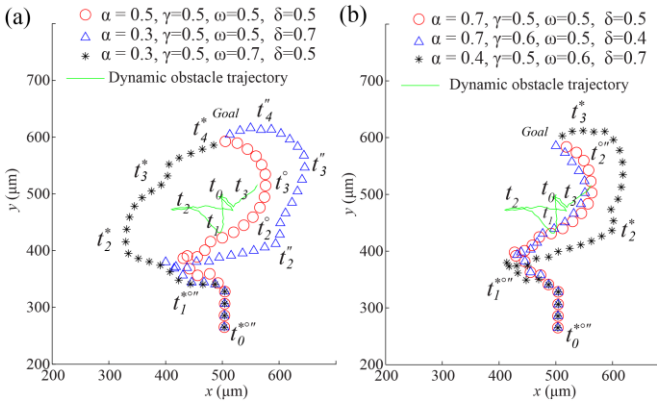

Figure 6. Simulation results showing different trajectories based on different weight values. (a) Path with different α, ω, and δ values, (b) Path with different α, γ, ω, and δ values (t^*: time for asterisk (black) trajectory, t^o: time for circle(red) trajectory, t'': time for triangle(blue) trajectory, number of 't' represents the same time)

However, similar path was generated between t_1 and t_3 if the weighting of the *head* function increases (Fig. 6(b)). In the case of $\alpha = 0.7$, the BPM's trajectory (red circle, blue triangle) have a much smaller curvature, as shown in Fig. 6(b). For simulations with similarly high δ, an increase of α results in a more aggressive trajectory (asterisk in Fig. 6(b)).

The simulation results confirm that the dynamic obstacle avoidance approach allows BPMs to avoid obstacles.

B. Experimental Setup

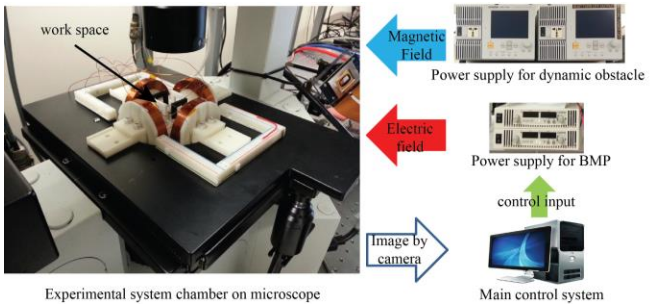

Figure 7. Experimental devices and control system

Our system is composed of a CCD camera mounted on an inverted microscope, a PDMS experimental chamber, and four power supplies. Two of power supplies are used to generate electric fields to control the BPMs on the *xy* plane. The others two power supplies are used to power the electromagnetic coil for controlling the magnetic dynamic obstacles. Fig. 7 shows the vision-based feedback control experimental setup. We used 45~50 µm paramagnetic beads as the dynamic obstacles.

C. Experimental Results for Magnetotaxis of BPMs

To confirm that magnetic field does have an influence on the BPMs, we observed the trajectories of self-actuated BPM under magnetic field for 5 min. Self-actuation motion of the same BPM has been observed with and without an applied magnetic field, as shown in Fig. 8(a) and 8(b), respectively. There is no qualitative difference with the presence of a magnetic field.

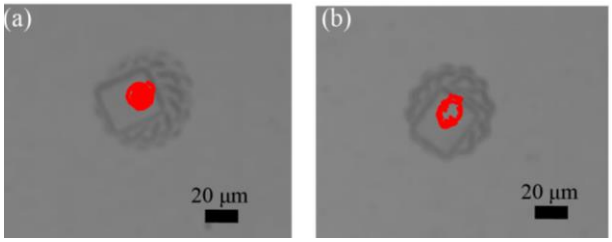

Figure 8. Self-actuation of BMPs. (a) Self-actuation without a magnetic field, (b) self-actuation under a magnetic field.

D. Experimental Results of Dynamic Obstacle Avoidance

The experiment was carried out using 30 µm × 32 µm rectangular BPMs and spherical magnetic particles in 50 µm diameter (as obstacles). The goal position was selected arbitrarily. The parameters for β_4 was 0.32 to initialize the dynamic window input. The weight values α, γ, ω, and δ were 0.5, 0.4, 0.4 and 0.5 respectively.

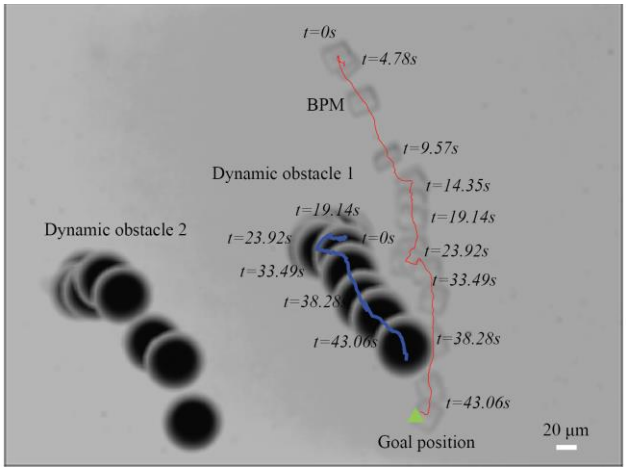

Figure 9.Experimental result with dynamic obstacles.

The moving obstacles were manually controlled toward the BPM using a magnetic field generated by a set of Maxwell coils for the *x* and *y* axes. The dynamic obstacle can have only 2D motion. The strength of magnetic field is fixed at 18 mT.

The BPM started to move down at first and the algorithm led the BPM to right side in order to clear the obstacle. The obstacle began to move at 19.14s. We tried to steer the obstacle to the BPM's position. As the obstacle approaches,

the algorithm calculated the optimal control input which allowed the BPM to successfully avoid the moving obstacle and reach the target position. The resulting trajectory of the BPM and the obstacles are depicted in Fig. 9. The input voltage for motion control in the experiment is described in Fig. 10. When the BPM was close to the first obstacle at around 10s in Fig. 9, the algorithm computed a strong value for the control input which tried to make the BPM move toward the empty area to the right. This result in making the BPM moved far away from the nearest obstacle during 10~20s as shown in Fig. 10. Once the obstacle moved toward the BPM at 33~44s, the computed control input made BPM move to the right side again.

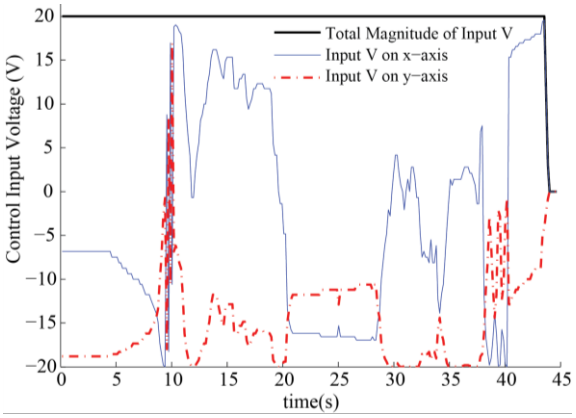

Figure 10. Control input voltages during experiment

V. CONCLUSIONS

In summary, we have demonstrated the possibility to develop a dynamic obstacle avoidance method for BPMs. There are several constraint elements to consider including the kinematics of the self-actuation motion. In addition, the motility of dynamic obstacle is stochastic. Thus, we combined an additional obstacle avoidance method, VFH, with the modified DWA method to reduce the probability of collision. Our algorithm chooses the optimal velocity from the admissible velocity space in order to avoid collision. The simulation result supports the presented algorithm for our robust collision avoidance algorithm. We further validated our algorithm through experimental result.

ACKNOWLEDGMENT

This work was funded by National Science Foundation (DMR 1306794), Korea Institute of Science Technology (K-GRL program), Korean Federation of Science and Technology Brainpool Fellowship and Army Research Office (W911NF-11-1-0490) awards to Min Jun Kim. The work of the third author Agung Julius has been supported in part by the National Science Foundation award (CMMI 1000284).

REFERENCES

[1] D. B. Weibel, DiLuzio, W.R., Whitesides, G.M., "Microfabrication meets microbiology," *Nat. Rev. Microbiol.,* vol. 5, pp. 209-218, 2007.

[2] J. P. Desai, Pillarisetti, A., Brooks, A.D., "Engineering approaches to biomanipulation," *Annu. Rev. Biomed, Eng.,* vol. 9, pp. 35-53, 2007.

[3] P. Y. Chiou, Ohta, A.T., Wu, M.C., "Massively parallel manipulation of single cells and microparticles using optical images," *Nature,* vol. 436, pp. 370-372, 2005.

[4] J. Castillo, Dimaki, M., Svendsen, W.E., "Manipulation of biological samples using micro and nano techniques," *Integr. Biol.,* vol. 1, pp. 30-42, 2009.

[5] M. Dauge, M. Gauthier, and E. Piat, "Modelling of a planar magnetic micropusher for biological cell manipulations," *Sensors and Actuators A: Physical,* vol. 138, pp. 239-247, 2007.

[6] E. B. Steager, Sakar, M.S., Kim, D.H., Kumar, V., Pappas, G., Kim, M.J., "Electrokinetic and optical control of bacterial microrobots," *J. Micromech. Microeng.,* vol. 21, p. 035001, 2011.

[7] M. S. Sakar, Steager, E.B., Kim, D.H., Julius, A.A., Kim, M.J., Pappas, G.J., Kumar, V., "Modeling, control and experimental characterization of microbiorobots," *Int. J. Robot. Res.,* vol. 30, pp. 647-658, 2011.

[8] F. Beyeler, A. Neild, S. Oberti, D. J. Bell, Y. Sun, J. Dual, *et al.*, "Monolithically fabricated microgripper with integrated force sensor for manipulating microobjects and biological cells aligned in an ultrasonic field," *Microelectromechanical Systems, Journal of,* vol. 16, pp. 7-15, 2007.

[9] J. Agnus, P. Nectoux, and N. Chaillet, "Overview of microgrippers and design of a micromanipulation station based on a MMOC microgripper," in *Computational Intelligence in Robotics and Automation, 2005. CIRA 2005. Proceedings. 2005 IEEE International Symposium on*, 2005, pp. 117-123.

[10] B. R. Donald, C. G. Levey, and I. Paprotny, "Planar microassembly by parallel actuation of MEMS microrobots," *Microelectromechanical Systems, Journal of,* vol. 17, pp. 789-808, 2008.

[11] J. Fang, K. Wang, and K. F. Bohringer, "Self-assembly of PZT actuators for micropumps with high process repeatability," *Microelectromechanical Systems, Journal of,* vol. 15, pp. 871-878, 2006.

[12] L. Zhang, J. J. Abbott, L. Dong, B. E. Kratochvil, D. Bell, and B. J. Nelson, "Artificial bacterial flagella: Fabrication and magnetic control," *Applied Physics Letters,* vol. 94, pp. 064107-064107-3, 2009.

[13] B. Behkam and M. Sitti, "Bacteria integrated swimming microrobots," in *50 years of artificial intelligence*, ed: Springer, 2007, pp. 154-163.

[14] B. Behkam and M. Sitti, "Bacterial flagella-based propulsion and on/off motion control of microscale objects," *Applied Physics Letters,* vol. 90, pp. 023902-023902-3, 2007.

[15] R. Di Leonardo, L. Angelani, D. Dell'Arciprete, G. Ruocco, V. Iebba, S. Schippa, *et al.*, "Bacterial ratchet motors," *Proceedings of the National Academy of Sciences,* vol. 107, pp. 9541-9545, 2010.

[16] M. S. Sakar, E. B. Steager, A. A. Julius, M. Kim, V. Kumar, and G. J. Pappas, "Biosensing and actuation for microbiorobots," in *Robotics and Automation (ICRA), 2010 IEEE International Conference on*, 2010, pp. 3141-3146.

[17] J. Ueda, L. Odhner, and H. H. Asada, "Broadcast feedback of stochastic cellular actuators inspired by biological muscle control," *The International Journal of Robotics Research,* vol. 26, pp. 1251-1265, 2007.

[18] A. A. Julius, M. S. Sakar, E. Steager, U. K. Cheang, M. Kim, V. Kumar, *et al.*, "Harnessing bacterial power in microscale actuation," in *Robotics and Automation, 2009. ICRA'09. IEEE International Conference on*, 2009, pp. 1004-1009.

[19] E. M. Purcell, "Life at low Reynolds number," *Am. J. Phys.,* vol. 45, pp. 3-11, 1977.

[20] E. Lauga and T. R. Powers, "The hydrodynamics of swimming microorganisms," *Reports on Progress in Physics,* vol. 72, p. 096601, 2009.

[21] J. Edd, S. Payen, B. Rubinsky, M. L. Stoller, and M. Sitti, "Biomimetic propulsion for a swimming surgical micro-robot," in *Intelligent Robots and Systems, 2003.(IROS 2003). Proceedings. 2003 IEEE/RSJ International Conference on*, 2003, pp. 2583-2588.

[22] M. S. Sakar, E. B. Steager, A. A. Julius, M. Kim, V. Kumar, and G. J. Pappas, "Modeling, control and experimental characterization of microbiorobots," *The International Journal of Robotics Research,* vol. 30, pp. 647-658, 2011.

[23] H. Kim, U. K. Cheang, M. J. Kim, and K. Lee, "Obstacle avoidance method for microbiorobots using electric field control," in *Cyber Technology in Automation, Control, and Intelligent Systems (CYBER), 2014 IEEE 4th Annual International Conference on*, 2014, pp. 117-122.

[24] T. R. Powers, "Role of body rotation in bacterial flagellar bundling," *Physical Review E,* vol. 65, p. 040903, 2002.

[25] E. B. Steager, M. S. Sakar, V. Kumar, G. J. Pappas, and M. J. Kim, "Electrokinetic and optical control of bacterial microrobots," *Journal of Micromechanics and Microengineering,* vol. 21, p. 035001, 2011.

[26] E. B. Steager, M. S. Sakar, V. Kumar, G. J. Pappas, and M. J. Kim, "Electrokinetic and optical control of bacterial microrobots," *J. Micromech. Microeng.,* vol. 21, p. 035001, 2011.

[27] D. Fox, W. Burgard, and S. Thrun, "The dynamic window approach to collision avoidance," *Robotics & Automation Magazine,* vol. 4, pp. 23-33, 1997.

[28] J. Borenstein and Y. Koren, "The vector field histogram-fast obstacle avoidance for mobile robots," *Robotics and Automation, IEEE Transactions on,* vol. 7, pp. 278-288, 1991.